European Radiology (2019) 29:13–21
https://doi.org/10.1007/s00330-018-5450-y

MUSCULOSKELETAL

Evaluation of MR-derived CT-like images and simulated radiographs compared to conventional radiography in patients with benign and malignant bone tumors

Alexandra S. Gersing[1] · Daniela Pfeiffer[1,2] · Felix K. Kopp[1] · Benedikt J. Schwaiger[1] · Carolin Knebel[3] · Bernhard Haller[4] · Peter B. Noël[1,2] · Marcus Settles[1] · Ernst J. Rummeny[1] · Klaus Woertler[1]

Received: 15 December 2017 / Revised: 8 March 2018 / Accepted: 26 March 2018 / Published online: 12 June 2018

Abstract

Objectives To evaluate the diagnostic value of MR-derived CT-like images and simulated radiographs compared with conventional radiographs in patients with benign and malignant bone tumors.

Methods In 32 patients with a benign or malignant bone lesion (mean age 33.9 ± 18.5 years, 17 females), 3-T MR imaging was performed including a 3D T1-weighted gradient echo sequence as the basis for the CT-like images. From these, intensity-inverted MR image volumes were converted into 2D images via a forward projection to obtain simulated radiographs. Two radiologists assessed these images as well as conventional radiographs for the type of periosteal reaction, matrix mineralization and destruction pattern. Agreement between the modalities was calculated using Cohen's κ.

Results The agreement between conventional radiographs and MR-derived CT-like images in combination with simulated radiographs was substantial (periosteal reaction, $\kappa = 0.67$; destruction pattern, $\kappa = 0.75$), and the sensitivity of both modalities for the final diagnosis of the lesion (aggressive vs. nonaggressive) was high (MR-derived CT-like images, 86.2% vs. conventional radiographs, 90.0%). Additional information on soft tissue extension (MR-derived CT-like images, 21.9% vs. conventional radiographs, 12.5%; $p = 0.009$) and lobulation (9.4% vs. 0%; $p < 0.001$) was significantly more often found on MR-derived CT-like images compared with conventional radiographs.

Conclusions The assessment of the destruction patterns, periosteal reaction and distinction between aggressive and nonaggressive tumors was feasible using MR-derived CT-like images and simulated radiographs and is comparable to that of conventional radiographs. Moreover, MR-derived CT-like images provided additional information on soft tissue extension and tumor architecture.

Key Points

- *CT-like images and simulated radiographs can be generated from 3D MRI.*
- *Evaluation of bone tumors is feasible with MR-derived images.*
- *CT-like images and simulated radiographs provide additional information on bone tumors*

Keywords Bone neoplasms · Magnetic resonance imaging · Musculoskeletal system · Diagnostic imaging · Joints

Alexandra S. Gersing and Daniela Pfeiffer contributed equally to this work.

✉ Alexandra S. Gersing
alexandra.gersing@ucsf.edu

[1] Department of Radiology, Klinikum rechts der Isar, Technical University of Munich, Klinikum rechts der Isar, Ismaninger Straße 22, 81675 Munich, Germany

[2] Chair for Biomedical Physics, Department of Physics & Munich School of BioEngineering, Technical University of Munich, Garching, Germany

[3] Department of Orthopaedic Surgery, Klinikum rechts der Isar, Technical University of Munich, Munich, Germany

[4] Institute of Medical Informatics, Statistics and Epidemiology, Technical University of Munich, Munich, Germany

Abbreviations

AP	Anterior-posterior
FOV	Field of view
GPU	Graphic processing unit
TE	Echo time
TR	Repetition time

Introduction

For the diagnosis of bone tumors, conventional radiographs are considered the suggested initial imaging modality, as emphasized by the American College of Radiology Appropriateness Committee [1, 2]. Radiography can accurately visualize the localization as well as the biologic activity of a bone lesion, which is reflected by the destruction pattern and the pattern of periosteal response [3]. Additionally, patterns of matrix mineralization, which might be detected by radiography, may be an important hint concerning the underlying histology [3–5]. In cases in which radiography fails because of superimposition or limited contrast resolution, as given in the spine or pelvis, radiography is replaced by computed tomography (CT) [6]. Nevertheless, the possibility to assess the patterns of bone destruction and periosteal response on MR imaging is desirable, because these features represent the basis for categorizing a bone lesion as aggressive or non-aggressive or even to establish a specific diagnosis and thus to set the course for further diagnostic work-up and therapy. It is well known that bone tumors can appear well defined on conventional MR images, while radiographs clearly depict an aggressive nature. This discrepancy might lead to erroneous assessments. Moreover, in addition to the evaluation of bone marrow and soft tissue, the assessment of bony structures by MR imaging with a validity comparable to radiographs would also be relevant in other skeletal disorders, such as infection, osteonecrosis, degenerative joint disease and trauma.

Recently, an approach has been suggested to derive images resembling radiographs from bone surface models based on 3D MR imaging data [7]. For the assessment of angles and joint space measurements in the ankle, good intrareader reproducibilities and agreement with conventional radiographs were found. However, the model only visualized bone surfaces based on a semi-automated segmentation of cortical bone, and no features of trabecular bone were depicted, thus excluding important information for potentially diagnosing benign and malignant bone tumors. Obtaining MR-based data of the entire bone structure, including the cancellous bone, visualized using 3D gradient echo MR imaging data with high contrast, may be a useful tool for the assessment of biologic activity of bone lesions and therefore for the optimization of the diagnosis of musculoskeletal tumors with the benefit of avoiding radiation exposure and additional examinations.

Aims of this study therefore were to evaluate (1) the image quality of MR-derived CT-like images and simulated radiographs in comparison with conventional radiographs, (2) the agreement between MR-derived images and conventional radiographs and (3) the sensitivity and specificity of MR-derived images for the distinction of benign and malignant bone tumors compared with conventional radiographs with the final diagnosis as standard of reference.

Materials and methods

Patient selection

Our institutional review board approved this study. Informed consent was obtained from all participants; the study was compliant with the Health Insurance Portability and Accountability Act. Participants were recruited from February 2015 until March 2016. In total, 32 consecutive patients (mean age 33.9±18.5 years, 17 females) with bone tumors or tumor-like bone lesions, for whom the final diagnosis was established and for whom conventional radiographs of the affected bone region as well as complete MR data sets were available, were included into this study. Benign (n = 18) and malignant (n = 14) bone lesions were either confirmed by biopsy (malignant tumors: 8 osteosarcomas, 1 Ewing sarcoma, 1 intraosseus angiosarcoma, 1 chondrosarcoma, 2 metastases and 1 lymphoma; benign tumors: 3 aneurysmal bone cysts, 1 giant cell tumor, 1 osteochondroma) or by consensus of clinical and imaging information (5 enchondromas, 3 non-ossifying fibromas, 2 osteoid-osteomas, 3 intraosseous lipomas). The lesions were localized as follows: at the femur (n = 14), tibia (n = 6), fibula (n = 2), humerus (n = 9) and ulna (n = 1).

MR imaging

MR imaging was performed on one 3-T MR scanner (Ingenia; Philips Healthcare, Best, The Netherlands) using a dedicated 8-channel shoulder, knee, extremity or foot/ankle coil (Medical Advances), respectively. A 3D T1-weighted gradient echo sequence was acquired with the following parameters: in-plane spatial resolution, 0.3 mm × 0.3 mm; TE, 2.715 ms; TR, 10 ms; flip angle, 8°; slice thickness, 0.5 mm; field of view (FOV) (range), 120 mm to 150 mm; acquisition time (range), 5 min 30 s to 6 min 45 s.

Post-processing

All post-processing steps were implemented and executed in MATLAB (MathWorks, Natick, MA). In a first step a mask of the surrounding background was segmented and in a second step inverted images were generated. The background mask

was computed with an in-house implementation of a 3D region growing with the seed point in the upper left corner of the first axial slice, since in our cases the scanned region was located in the center of the FOV and the position in the upper left corner always belonged to the background. To avoid that the mask grew into a region containing tissue, the threshold for region growing was set to an intensity value of two, meaning that pixels with intensity differences greater than twice the mean intensity of pixels in the mask were excluded. At the end, pixels belonging to the background were set to zero and the other pixels were set to one. Inverted MR images were multiplied point-wise with the background mask. After this step, the images resembled CT images: the surrounding background was zero and bone showed the highest signal intensities. To generate the 2D projection image of bone, the contrast between bone and soft tissue was increased using the MATLAB integrated function "adapthisteq", which applies contrast-limited adaptive histogram equalization to enhance the contrast of the inverted images. This step especially increases the contrast of small objects and results in better distinction between calcified and non-calcified tissue. Moreover, the guided image filter was applied under self-guidance for edge-preserving smoothing [8], leading to more homogeneous images with lower intensity outliers that would disturb the forward projection. As a final processing step, we chose the n-th power of the contrast-enhanced images, with a larger number resulting in greater intensity differences between bone and soft tissues. All data in this work were processed with $n = 10$. To compute 2D projection images from the processed 3D data, forward projection, in the geometry of a conventional X-ray system, was performed using a cone-beam projector from our in-house-developed CT reconstruction suite. The processing chain comprising all previously described steps was fully automated without any user interaction. The average total automatic processing time took 4.73 ± 2.45 min per examination, depending on the field of view, including reading and processing the DICOM files with MATLAB.

Image analysis

MR-derived CT-like images and simulated radiographs were individually and independently read by two radiologists (K.W. and A.S.G. with 22 and 4 years of experience in musculoskeletal radiology, respectively), blinded to clinical information and all other patient information including all MR sequences other than the 3D gradient-echo sequence used for this analysis. Radiologists read the images in a random order. The exact location of the lesion within the affected bone was assessed in respect to the transverse plane (central, intracortical, periosteal, and parosteal). The destruction pattern was graded using the Lodwick classification system (Table 1 [9]). Images were graded for sharpness, noise and overall image quality on a four-point Likert scale (score of 1, excellent; 2, good; 3, moderate; 4, poor). The images were evaluated for the presence and type of periosteal reaction as well as matrix mineralization. The extent of cortical remodeling and expansion (none, endosteal scalloping, neocortex) and the type of periosteal reaction (none, continuous, interrupted, complex) were assessed, whereas the continuous and interrupted periosteal reactions were further classified as solid, single layer, multilayered or spiculated. Moreover, the type of tumor matrix mineralization (chondrogenic, osteogenic, ground glass) was assessed. Additional findings, such as the presence of an extraosseous soft tissue component and tumor architecture (lobulation), were evaluated. After at least 14 days the same features were evaluated on conventional radiographs by both radiologists blinded to clinical information.

Statistical analysis

The data were analyzed by an experienced statistician (B.H.), using IBM SPSS Statistics for Windows, version 23.0 (IBM Corp., Armonk, NY, USA). All statistical tests were performed two sided, and a level of significance (α) of 0.05 was used for all tests. For comparison of characteristics between malignant and benign lesions, Fisher's exact test was used for categorical data, the independent samples t test for numerical, approximately normally distributed data and the Mann-Whitney U test for skewed numerical data. The Wilcoxon signed-rank test was used to calculate differences in diagnostic image quality between conventional radiographs and MR-derived CT-like images in combination with simulated radiographs assessed using the Likert scale. The agreement between the MR-derived CT-like images in combination with simulated radiographs and conventional radiographs was calculated using Cohen's kappa. The inter- and intraobserver reliability of the assessment of the MR-derived CT-like images and simulated radiographs and the assessment of the conventional radiographs was also calculated using

Table 1 Classification of Bone Lesions

Type	Pathologic finding
IA	Geographic lesion, sharp margin with a sclerotic rim, expansion of cortex ≤ 1cm
IB	Geographic lesion, unsharp margin with or without a sclerotic rim, expansion of cortex > 1 cm
IC	Geographic lesion, unsharp margin without a sclerotic rim with penetration of the cortex, partial or total penetration of the cortex possible
II	Moth-eaten lesion, unsharp margin without a sclerotic rim with partial or total penetration of the cortex
III	Permeated lytic lesion without geographic component, with partial or total penetration of the cortex

Note: According to the Classification of Lodwick et al. [9]

Cohen's kappa. Intraobserver reliability was based on a second evaluation of all conventional radiographs and MR-derived CT-like images by both radiologists in combination with simulated radiographs with at least 4 weeks after the first assessments [10]. The values can be interpreted as poor (0), slight (0.0–0.2), fair (0.21–0.40), moderate (0.41–0.60), substantial (0.61–0.80) and almost perfect (0.81–1.00) [11]. Sensitivity and specificity of the ability of conventional radiographs and MR-derived CT-like images to categorize a bone lesion into aggressive and nonaggressive lesions based on the final diagnosis were calculated for each reader. Comparisons of these measures were performed using McNemar's test after stratification of the data for aggressive/nonaggressive lesions. For all measures, 95% confidence intervals (CI) were calculated.

Results

Patient characteristics and image quality

Between patients with benign and malignant bone lesions, no significant differences were found regarding age (patients with benign lesions, 31.3 ± 14.7 years versus patients with malignant lesions, 37.2 ± 22.9 years; $p = 0.41$) and sex (patients with benign lesions, 10 female (55.6%) versus patients with malignant lesions, 7 female (50.0%); $p = 0.41$). All bone lesions (32/32, 100%) were apparent on MR-derived CT-like images, simulated radiographs and conventional radiographs. The diagnostic image quality was not rated significantly different on conventional radiographs [median 3 (range: 1, 4)] and simulated radiographs [median 3 (range: 1, 4); $p = 0.84$] or on MR-derived CT-like images [median 3 (range: 2, 4) vs. conventional radiographs, $p = 0.71$].

Table 2 Frequency [*n* (%)] of the evaluation criteria depicted on conventional radiographs by radiologist 1

Location	
Central	29 (90.6)
Intracortical	1 (3.1)
Periosteal	2 (6.3)
Parosteal	0 (0.0)
Lodwick classification	
IA	7 (21.9)
IB	11 (34.4)
IC	2 (6.3)
II	7 (21.9)
III	5 (15.6)
Expansion	
None	19 (59.4)
Endosteal	5 (15.6)
Scalloping	8 (25.0)
Periosteal reaction	
None	20 (62.5)
Continuous	4 (12.5)
Interrupted	4 (12.5)
Complex	4 (12.5)
Matrix mineralization	
Chondrogenic	3 (9.4)
Osteogenic	6 (18.8)
Ground glass	0 (0.0)
Lesion architecture	
Lobulation	0 (0.0)

Image analysis

The frequencies of each evaluation criterion assessed on conventional radiographs are listed in Table 2. The MR-derived

Table 3 Agreement between MR-derived simulated radiographs and conventional radiographs and inter- and intraobserver agreement*

	Agreement between MR-derived simulated data sets and conventional radiographs		Inter- and intraobserver agreement			
	Radiologist 1[1]	Radiologist 2[1]	MR-derived simulated data sets		Conventional radiographs	
			Interobserver[2]	Intraobserver[3]	Interobserver[2]	Intraobserver[3]
Location	1.00 [1.00, 1.00]	1.00 [1.00, 1.00]	1.00 [1.00, 1.00]	1.00 [1.00, 1.00]	1.00 [1.00, 1.00]	1.00 [1.00, 1.00]
Lodwick classification	0.75 [0.56, 0.91]	0.67 [0.46, 0.86]	0.87 [0.71, 1.00]	0.91 [0.78, 1.00]	0.88 [0.72, 1.00]	1.00 [1.00, 1.00]
Expansion	0.90 [0.77, 1.00]	0.71 [0.46, 0.90]	0.76 [0.56, 0.95]	0.76 [0.56, 0.94]	0.85 [0.66, 1.00]	1.00 [1.00, 1.00]
Periosteal reaction	0.67 [0.45, 0.88]	0.59 [0.40, 0.79]	0.89 [0.73, 1.00]	1.00 [1.00, 1.00]	0.83 [0.63, 1.00]	0.89 [0.74, 1.00]
Matrix mineralization	0.87 [0.64, 1.00]	0.87 [0.64, 1.00]	1.00 [1.00, 1.00]	1.00 [1.00, 1.00]	1.00 [1.00, 1.00]	1.00 [1.00, 1.00]

*Data in brackets are 95% confidence intervals

[1] Agreement between MR-derived simulated radiographs and conventional radiographs calculated using Cohen's κ coefficient

[2] Interobserver agreement for MR-derived simulated radiograph and conventional radiograph analyses using the Cohen's κ coefficient

[3] Intraobserver agreement for MR-derived simulated radiograph and conventional radiograph analyses using the Fleiss κ

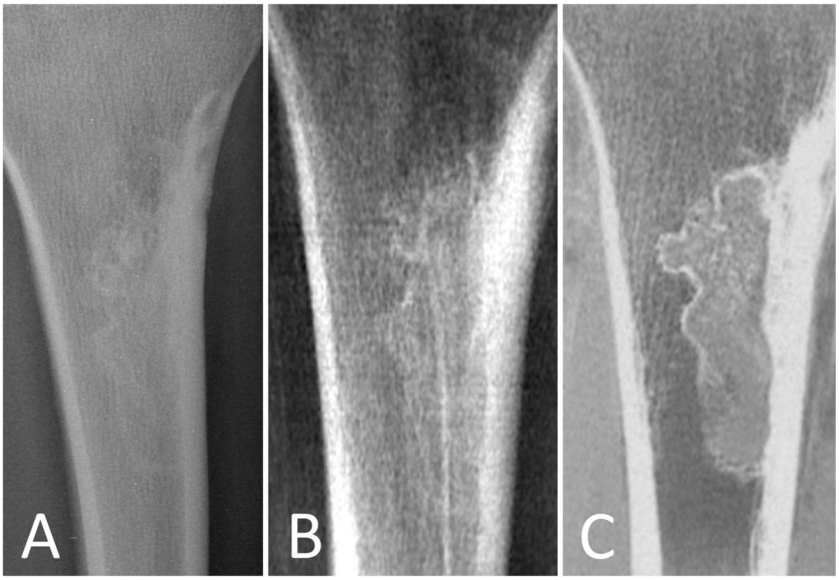

Fig. 1 Typical non-ossifying fibroma of the proximal tibia in a 24-year-old female patient. (**A**) The conventional AP radiograph shows a cortically based metaphyseal lesion with a lobulated contour and sclerotic margin (Lodwick grade IA) and absence of periosteal reaction. The same morphologic features are demonstrated by (**B**) the MR-derived simulated AP radiograph and (**C**) the coronal 2-mm section from the MR-derived CT-like images

CT-like images in combination with simulated radiographs showed a substantial to almost perfect agreement with conventional radiographs for both radiologists [e.g., Lodwick classification, κ of 0.75 (95% CI, 0.56, 0.91) and 0.67 (95% CI, 0.46, 0.86); matrix mineralization, κ of 0.87 (95% CI, 0.64, 1.00) and 0.87 (95% CI, 0.64, 1.00); Table 3; Fig. 1]. Furthermore, the agreement of MR-derived CT-like images with conventional radiographs and of MR-derived simulated radiographs with conventional radiographs also showed a substantial to perfect agreement for both radiologists (Table 4).

The intra- and interobserver agreement for both conventional radiographs and MR-derived CT-like images in combination with simulated radiographs were substantial to perfect (κ ranging between 0.63 and 1.00; Table 3; Fig. 2). The intra- and interobserver agreement for both MR-derived CT-like images and simulated radiographs separately were also substantial to perfect (κ ranging between 0.60 and 1.00).

Additional information on soft tissue extension (MR-derived CT-like images, 21.9% vs. conventional radiographs, 12.5%; Figs. 3 and 4) and tumor architecture (lobulation of bone tumor, 9.4% vs. 0%; Fig. 5) was found significantly more often on MR-derived CT-like images compared with conventional radiographs. Moreover, the endosteal scalloping of cortical bone was detected more often on MR-derived CT-like images compared with conventional radiographs (MR-derived images, 9.4% vs. conventional radiographs, 0%).

Sensitivity and specificity with final diagnosis as standard of reference

The sensitivity and specificity of MR-derived CT-like images in combination with simulated radiographs with the final diagnosis of the bone lesion by either histology or consensus between clinical and imaging information into aggressive vs. nonaggressive lesions was comparable to those of conventional radiographs for both observers, with a sensitivity of 0.86 (95% CI, 0.65, 1.00) for MR-derived CT-like images in combination with simulated radiographs and sensitivity of 0.90

Table 4 Separate analysis of agreement between MR-derived CT and conventional radiographs as well as between MR-derived simulated radiographs only and conventional radiographs

	Agreement between MR-derived CT and conventional radiographs		Agreement between MR-derived simulated radiographs and conventional radiographs	
	Radiologist 1[1]	Radiologist 2[1]	Radiologist 1[1]	Radiologist 2[1]
Location	1.00 [1.00, 1.00]	1.00 [1.00, 1.00]	1.00 [1.00, 1.00]	1.00 [1.00, 1.00]
Lodwick classification	0.79 [0.62, 0.96]	0.75 [0.58, 0.93]	0.75 [0.58, 0.93]	0.72 [0.53, 0.90]
Expansion	0.76 [0.57, 0.95]	0.71 [0.51, 0.92]	0.79 [0.59, 0.98]	0.78 [0.60, 0.98]
Periosteal reaction	0.83 [0.65, 1.00]	0.70 [0.47, 0.94]	0.82 [0.62, 1.00]	0.70 [0.45, 0.94]
Matrix mineralization	0.81 [0.61, 1.00]	0.74 [0.51, 0.98]	0.93 [0.80, 1.00]	0.79 [0.57, 1.00]

Data in brackets are 95% confidence intervals

[1] Agreement between MR-derived simulated radiographs and conventional radiographs calculated using Cohen's κ coefficient

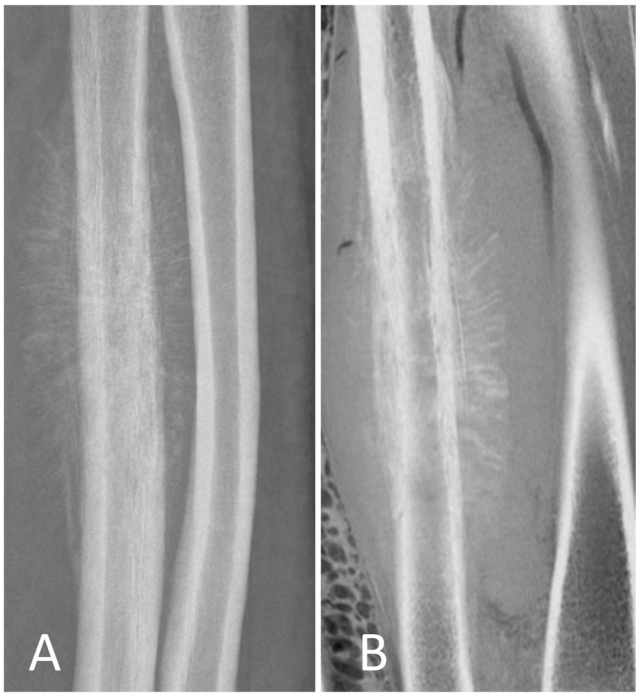

Fig. 2 Histologically confirmed Ewing sarcoma of the ulna in a 27-year-old female patient. A permeative diaphyseal lesion (Lodwick grade III) accompanied by complex periosteal reaction is depicted on both (**A**) the conventional AP radiograph and (**B**) the MR-derived simulated AP radiograph

(95% CI, 0.67, 1.00) for conventional radiographs. The specificity for MR-derived CT-like images in combination with simulated radiographs was 1.00 (95% CI, 0.90, 1.00) and was 1.00 (95% CI, 0.90, 1.00) for conventional radiographs (Table 5).

Discussion

In our study, the agreement between conventional radiographs and MR-derived CT-like images in combination with simulated radiographs was substantial to almost perfect, and the sensitivity and specificity of both modalities with the final diagnosis of the bone tumor (aggressive vs. nonaggressive) were comparable. In particular, the assessment of the destruction patterns and periosteal reaction allowing the distinction between aggressive and nonaggressive tumors, confirmed by either histology or by the consensus of radiologic and clinical findings, seemed feasible using MR-derived images and was comparable to conventional radiographs. Moreover, the MR-derived CT-like images provided additional information on soft tissue extension and tumor architecture.

The information of the biologic activity of bone tumors yielded by MR-derived CT-like images and simulated radiographs showed an equivalent diagnostic value compared with conventional radiographs. It needs to be emphasized that radiographs present the current standard in imaging of bone lesions [1, 2]. Therefore, in our study, we assessed imaging features of biologic activity obtained from MR-derived CT-like images and simulated radiographs with conventional radiographs as reference standard. Moreover, the agreement of both modalities with the final histologic and clinical diagnosis was assessed separately.

In general, MR imaging is an accepted method to visualize bone lesions to narrow the differential diagnoses and to evaluate the extent of bone lesions for local staging. The combination of the assessment of these features and the osseous destruction pattern and periosteal reaction in addition has several advantages. In our study, the performance of MR-derived CT-like images and simulated radiographs was comparable regarding the assessment of the biologic activity of bone tumors. While CT-like images provided additional information, e.g., on extraosseus components, we believe that generating simulated radiographs is an important component of the presented method. In clinical routine, the assessment of bone lesions is performed on conventional radiographs using classification systems that have been developed for radiography and that cannot be directly transferred to CT. Furthermore, we

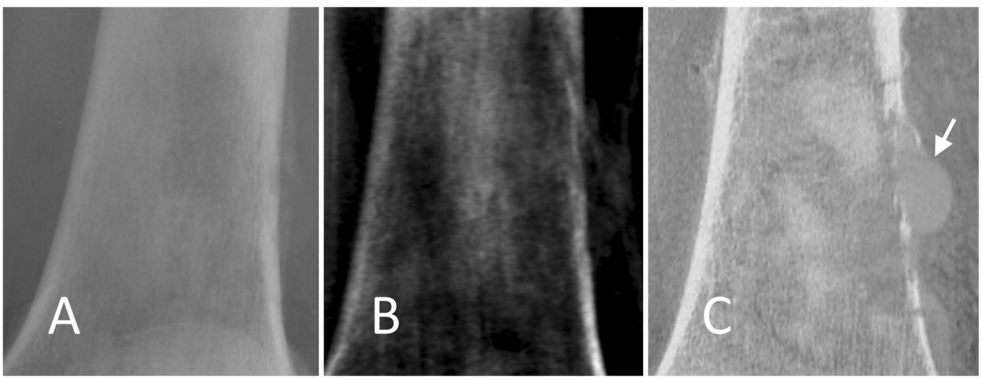

Fig. 3 Histologically confirmed undifferentiated high-grade pleomorphic bone sarcoma of the distal femur in a 43-year-old male patient. (**A**) The conventional AP radiograph shows a geographic lytic lesion with moth-eaten bone destruction (Lodwick II) and an interrupted periosteal reaction. The same aggressive morphology is seen on (**B**) the MR-derived simulated AP radiograph. (**C**) Coronal 2-mm section from the MR-derived CT-like images additionally shows extra-osseous soft tissue component (arrow)

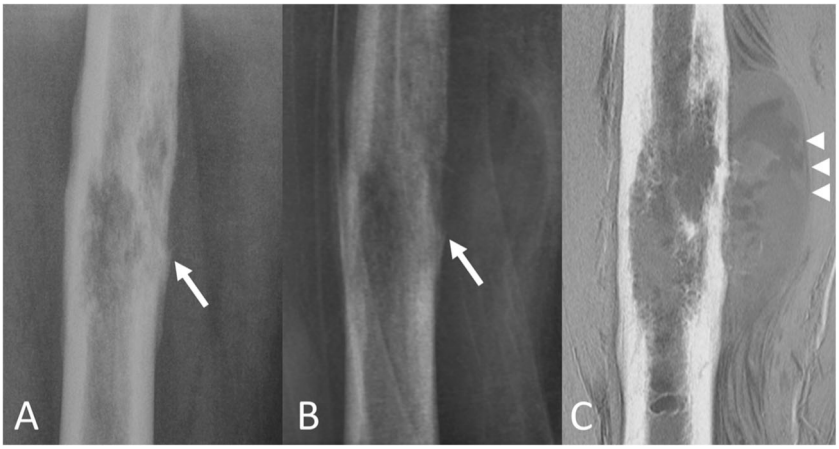

Fig. 4 Histologically confirmed osteosarcoma of the femur in a 28-year-old female patient. (**A**) The conventional AP radiograph shows a lytic lesion with moth-eaten bone destruction (Lodwick II) and an interrupted periosteal reaction (white arrows). The same aggressive morphology is seen on (**B**) the MR-derived simulated AP radiograph. (**C**) Coronal 2 mm-section from the MR-derived CT-like images additionally show a large extra-osseous soft tissue component (arrowheads)

believe, that it is important to deliver radiograph-like images to referring physicians and orthopedic surgeons rather than a CT-like data set, even if the radiologist might prefer to analyze the CT-like images.

To our best knowledge, this is the first study to evaluate the clinical value of MR-derived CT-like images and simulated radiographs in musculoskeletal tumor imaging. In a previous study, Nordeck et al. presented a method to derive images resembling radiographs from bone surface models based on 3D MR imaging data [7]. Based on a volume-rendered reconstruction of a 3D proton-density weighted isotropic turbo spin echo sequence, the cortical bone was segmented in a semiautomatic fashion and then captured in standard projections. Nevertheless, in this previous study, the simulated radiographs were obtained only from the bone surface and only cortical bone was segmented. Therefore, no information about trabecular bone or any other feature of central pathologies, such as the destruction pattern or matrix mineralization, could potentially be assessed with this previous method. In contrast, in our study, the MR-derived CT-like images and simulated radiographs were generated by enhancing the contrast of all structures visualized with gradient echo sequences, including subcortical bone structures. In addition, it has been shown that gradient echo sequences, as used in our study, are superior to spin echo sequences for bone imaging regarding their signal-to-noise ratio and contrast [12]. Our simulation method imitates the spatial setup of a conventional x-ray unit, with a comparable virtual tube-detector distance, detector size and x-ray cone beam angle, which makes the simulated radiographs based on MR imaging even more similar to the original conventional radiographs. This may be especially beneficial for measurements performed on the simulated radiographs and makes image analysis more intuitive. This specific 3D T1 gradient echo sequence was chosen because it provides superior contrast particularly between calcified and non-calcified tissues, while other tissue contrasts are minimal compared with other susceptibility-weighted pulse sequences. This is especially important for the assessment of cancellous bone and destruction patterns in patients with bone lesions. To be sensitive to susceptibility with reasonable scan times, gradient echo imaging is mandatory. Moreover, the T1-weighted gradient echo sequence we used showed fewer artifacts compared with T2*-weighted gradient echo sequences and also had excellent spatial resolution while maintaining adequate scan times. It is possible that different parameter choices

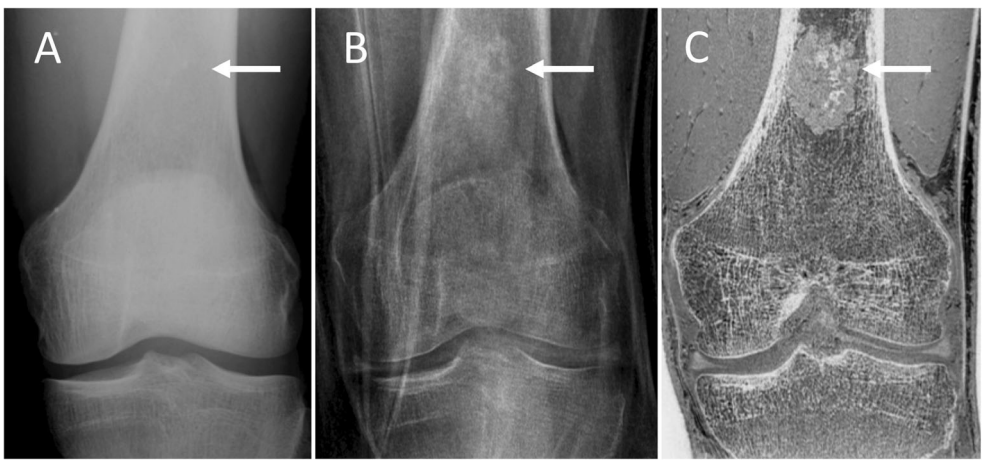

Fig. 5 Enchondroma of the distal femur in a 41-year-old male patient. (**A**) The conventional AP radiograph shows stippled matrix mineralizations (arrows) in the center of the metaphysis within a hardly visible lytic lesion. (**B**) The MR-derived simulated AP radiograph and (**C**) the coronal 2-mm section from the MR-derived CT-like data set demonstrate a well-defined medullary lesion with a lobulated contour and typical chondrogenic matrix mineralizations

Table 5 Sensitivity and specificity of MR-derived simulated radiographs or conventional radiographs for the final diagnosis (aggressive vs. nonaggressive lesions) for each radiologist

	Radiologist 1		Radiologist 2	
	MR-derived simulated data sets	Conventional radiographs	MR-derived simulated data sets	Conventional radiographs
Sensitivity	0.86 [0.56, 1.00]	0.90 [0.68, 1.00]	0.86 [0.58, 1.00]	0.90 [0.67, 1.00]
Specificity	1.00 [0.90, 1.00]	1.00 [0.90, 1.00]	1.00 [0.90, 1.00]	1.00 [0.90, 1.00]

Data in brackets are 95% confidence intervals.

may produce similar or even improved image quality, which needs to be assessed in future studies.

MR imaging is accepted as the most valuable method for the evaluation of the extent and extraosseus/soft tissue components of bone tumors, while it is still considered less specific regarding the final diagnosis compared with conventional radiographs or CT [2, 13–15]. MR imaging of bone lesions was limited by the inferior capability to assess the involved bone itself and its response to an intraosseous process. In this context, the new technique presented in our study may be a useful additional tool for musculoskeletal MR imaging to provide information comparable to conventional radiographs regarding the biologic activity of bone lesions, while patients may be spared an additional examination. This is particularly beneficial for young patients with benign lesions, since in these patients multiple long-term follow-up examinations may be required for lesion monitoring, cumulatively leading to substantial radiation exposure. In addition to the regular information on the destruction pattern and periosteal reaction, the MR-derived simulated radiograph data also provided additional information on the tumor matrix as well as soft tissue extension. Overall, MR imaging could provide an evaluation of the soft tissue and bone structure of bone lesions within the same examination, thus facilitating the diagnosis and therapy planning of bone tumors, with the benefits of being able to easily apply standard clinical cross-referencing tools for image analysis and simultaneous acquisition of MR images as well as MR-derived CT- and radiograph-like images [16].

Our study has limitations. MR-derived simulated radiographs were generated with an automated computerized algorithm. For this post-processing step, dedicated workstations are needed that are not part of the regular clinical setup. The total automatic processing time took roughly 5 min per examination. This time may be shortened in the future through the optimization of algorithms for graphic processing unit (GPU) usage. Moreover, it needs to be noted that no extra processing time was needed for the MR-derived CT-like images and that these could be interpreted by simply inversing the intensity on the PACS work station. This study assessed the feasibility of the presented method in a first, relatively small patient cohort with different benign and malignant bone lesions. Further validation studies in larger cohorts and using CT are needed to assess the actual value of the presented method for the workflow in centers diagnosing and treating patients with different bone tumors.

In summary, our study showed that CT-like images and simulated radiographs derived from 3D gradient echo MR imaging showed an imaging quality equivalent to conventional radiographs. Moreover, the assessment of bone lesions using these MR-derived CT-like images in combination with the simulated radiographs showed substantial agreement with conventional radiographs regarding imaging features as well as a comparably high specificity and sensitivity for the differentiation between aggressive and nonaggressive bone lesions, as confirmed by histology or consensus between clinical and imaging information. The MR-derived CT-like images provided additional information on the tumor matrix mineralization and soft tissue extension. Therefore, MR-derived CT-like images in combination with the simulated radiographs may become a valuable component of MR imaging protocols for bone lesions in the future.

Acknowledgements This work was presented as a scientific presentation at the 4th Annual Meeting of the German Society of Musculoskeletal Radiology in Berlin (April 2018).

Funding The authors state that this work has not received any funding.

Compliance with ethical standards

Guarantor The scientific guarantor of this publication is Dr. Klaus Woertler, M.D.

Conflict of interest The authors of this manuscript declare no relationships with any companies, whose products or services may be related to the subject matter of the article.

Statistics and biometry One of the authors, Dr. Bernhard Haller, Ph.D., has significant statistical expertise.

Informed consent Written informed consent was obtained from all patients in this study.

Ethical approval Institutional Review Board approval was obtained.

Methodology
- prospective
- diagnostic or prognostic study
- performed at one institution

References

1. Mintz DN, Hwang S (2014) Bone tumor imaging, then and now: review article. HSS J 10:230–239
2. Morrison WB, Weissman BN, Kransdorf MJ et al (2013) ACR Appropriateness Criteria®; primary bone tumors
3. Madewell JE, Ragsdale BD, Sweet DE (1981) Radiologic and pathologic analysis of solitary bone lesions. Part I: internal margins. Radiol Clin North Am 19:715–748
4. Ragsdale BD, Madewell JE, Sweet DE (1981) Radiologic and pathologic analysis of solitary bone lesions. Part II: periosteal reactions. Radiol Clin North Am 19:749–783
5. Sweet DE, Madewell JE, Ragsdale BD (1981) Radiologic and pathologic analysis of solitary bone lesions. Part III: matrix patterns. Radiol Clin North Am 19:785–814
6. Miller TT (2008) Bone tumors and tumorlike conditions: analysis with conventional radiography. Radiology 246:662–674
7. Nordeck SM, Koerper CE, Adler A et al (2017) Simulated radiographic bone and joint modeling from 3D ankle MRI: feasibility and comparison with radiographs and 2D MRI. Skeletal Radiol 46: 651–664
8. He K, Sun J, Tang X (2013) Guided image filtering. IEEE Trans Pattern Anal Mach Intell 35:1397–1409
9. Lodwick GS, Wilson AJ, Farrell C, Virtama P, Dittrich F (1980) Determining growth rates of focal lesions of bone from radiographs. Radiology 134:577–583
10. Fleiss JL, Cohen J (1973) The Equivalence of Weighted Kappa and the Intraclass Correlation Coefficient as Measures of Reliability. Educational and Psychological Measurement 33:613–619
11. Fleiss JL (1971) Measuring nominal scale agreement among many raters. Psychological Bulletin 76:378–382
12. Schmalbrock P (2000) Comparison of three-dimensional fast spin echo and gradient echo sequences for high-resolution temporal bone imaging. J Magn Reson Imaging 12:814–825
13. Woertler K (2003) Benign bone tumors and tumor-like lesions: value of cross-sectional imaging. Eur Radiol 13:1820–1835
14. Panicek DM, Gatsonis C, Rosenthal DI et al (1997) CT and MR imaging in the local staging of primary malignant musculoskeletal neoplasms: Report of the Radiology Diagnostic Oncology Group. Radiology 202:237–246
15. Norton KI, Hermann G, Abdelwahab IF, Klein MJ, Granowetter LF, Rabinowitz JG (1991) Epiphyseal involvement in osteosarcoma. Radiology 180:813–816
16. Nemec SF, Donat MA, Mehrain S et al (2007) CT-MR image data fusion for computer assisted navigated neurosurgery of temporal bone tumors. Eur J Radiol 62:192–198